

In Situ Measurements of Bridged Crack Interfaces in the Scanning Electron Microscope

Jürgen Rödel,* James F. Kelly,* and Brian R. Lawn*

Ceramics Division, National Institute of Standards and Technology, Gaithersburg, Maryland 20899

A device for in situ SEM examination of crack propagation during loading of compact tension specimens is described, with a specific demonstration on an alumina ceramic. The device facilitates direct qualitative observations of the inception and subsequent frictional pullout of grain-localized bridges at the crack interface. Quantitative data on the bridging mechanism are obtained from measurements of the crack-opening displacements behind the crack tip. The crack profile is found to be closer to linear than parabolic at the bridged interface. Deconvolution of these crack-opening data allow for an evaluation of the closure tractions operative at the crack walls within the bridging zone, and thence the *R*-curve. [Key words: scanning electron microscopy, cracks, bridging, pullout, toughness.]

I. Introduction

THE achievement of respectable fracture toughness in brittle ceramics necessitates the incorporation of crack-tip shielding agents like frontal-zone phase transformations¹ or microcracking,² crack-interface fiber pullout,³ or interlocking grain sliding.^{4,5} A proper understanding of the constitutive micromechanics of such processes can be gained only by direct observation of the crack shielding zone at the microstructural level during loading (and unloading, where applicable). In aluminas, for instance, in situ optical microscopy has been used to identify crack-interface grain bridging as the primary cause of *R*-curve toughening,^{4,6} a mechanism that had passed unnoticed in previous, conventional post-mortem surface fractography. But while those studies have led to working microstructural constitutive relations for *R*-curve modeling of crack-interface bridging in simple monophase ceramics,^{5,7} finer elements of the restraining mechanisms remain obscure. Optical microscopy is severely limited in its capacity to discern critical details of grain pullout and detachment. It is even more restrictive as a quantitative tool: in typical microstructures the crack-wall separations at the bridged interface are on the order of 1 μm or less.

Accordingly, we have custom-designed a device for in situ crack observations in the scanning electron microscope (SEM). Previous SEM straining fixtures for tensile specimens or bend bars⁸⁻¹⁰ have demonstrated the feasibility of the approach. Our device allows one to follow the progress of crack propagation at relatively high magnification in compact tension specimens with externally controlled loading, and thence to gain quantitative insight into the underlying *R*-curve processes.

R. F. Cook—contributing editor

Manuscript No. 197881. Received December 20, 1989; approved June 22, 1990.

Presented at the 92nd Annual Meeting of the American Ceramic Society, Dallas, TX, April 25, 1990 (Basic Science and Engineering Ceramics Divisions, Paper No. 2-JXX-90).

Supported by the U. S. Air Force Office of Scientific Research.

*Member, American Ceramic Society.

*On leave from the Department of Materials Science and Engineering, Lehigh University, Bethlehem, PA.

In this paper we briefly describe the fixture and illustrate its potential by tests on a polycrystalline alumina with demonstrated *R*-curve characteristics. Micrographs depicting the evolution of interlocking grain sites are presented as illustrations of the capacity to resolve essential microstructural detail at the bridged crack interface. Crack-opening displacement (COD) measurements are made along the bridging zone during the crack evolution. Corresponding bridging stresses in the crack wake are deconvoluted from these measurements, as functions of both COD and crack-plane coordinate. From these functions, we determine the *R*-curve characteristics for our particular material/geometry system.

II. SEM Crack Propagation Studies

(1) SEM Device

Essential details of the SEM crack propagation device are shown in the schematic of Fig. 1. The device allows remote electronic application and monitoring of the applied load. Extension of a piezoelectric translator T delivers an opening force to the specimen S via pivot arms P and loading arms L. The P arms are connected to the L arms by ball-bearing joints and to the base of the device by pin joints for maximum flexibility. A load cell C mounted in one of the L arms measures the transmitted force. The piezoelectric translator is activated by a high-voltage amplifier which, in conjunction with a function generator, allows application of any prescribed load-time function (including, potentially, cyclic). The device operates effectively as a "soft" machine: that is, crack extension occurs under nearly constant load.

The entire fixture is housed within the chamber of an SEM.[†] Crack-interface events during externally controlled loading

[†]Amray 1830, Amray, Inc., Bedford, MA.

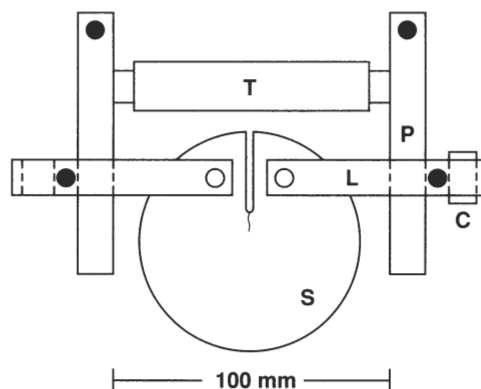


Fig. 1. Schematic of device for in situ SEM observations of fracture specimen under load: (T) piezoelectric translator, (C) load cell, (P) pivot arms, (L) loading arms, (S) specimen. Solid circles indicate joints between pivot arms and loading arms and between pivot arms and base.

can be viewed in real time and are routinely taped on a video recording unit for closer study.

A more detailed description of the unit will be given elsewhere.¹¹

(2) Crack Propagation Specimens

Alumina disks 4 mm thick and 100 mm in diameter were prepared by hot-pressing fine powder (nominal particle size $0.5\ \mu\text{m}$),[†] without additives, at 1650°C for 3 h at 35 MPa under vacuum. The pressed material was nonporous ($>99.9\%$ density), and the microstructure was equiaxed with a grain size of $11\ \mu\text{m}$. The disks were ground to 1-mm thickness and the prospective viewing surface polished with diamond paste to $1\text{-}\mu\text{m}$ finish.

Notches were sawed and loading holes drilled in the disks to form compact-tension specimens. The distance from the load points to the crack plane was 7 mm and from the line of the loading arms to the initial notch tip 15 mm. The notch root radius was $150\ \mu\text{m}$. To enhance stability in the initial crack extension the notch was cut at an angle 28° to the surface in quasi-chevron geometry, i.e., so that the tip extended some 2 mm farther on the unpolished side. A Vickers indentation starter crack of diameter $\approx 240\ \mu\text{m}$ (load 50 N) was then placed in the polished surface with its center $200\ \mu\text{m}$ in front of the notch, in alignment with the notch plane. This starter crack was made to pop in some $300\ \mu\text{m}$ beyond the indentation center in a preliminary load cycle. The notch was then resawed through the indentation, leaving a precrack $\approx 100\ \mu\text{m}$ long. After the first crack propagation run through $\approx 2\ \text{mm}$ (i.e., through to the end of the chevron) the specimen was removed and resawed, for second and third runs.

Some soda-lime glass specimens were also prepared to similar dimensions, as non-*R*-curve controls. After the notch was sawed, these specimens were annealed for 1 h at 550°C to remove residual stresses.

Specimens were gold coated before testing in the SEM. The evolution of bridging grains at selected sites in the crack wake was followed as the crack tip advanced. Video recordings were made along the interfaces at each of the fully propagated cracks for profile measurements. The COD measurements themselves were made only in well-behaved regions, e.g., at grain facets oriented normal to the load axis and located away from any secondary cracking around bridging sites. The cracks were rendered highly visible in the secondary electron mode by edge charging. This charging limited the absolute resolution of surface-surface separations to about 70 nm, although relative measurements could be made to better than 30 nm.

III. Results

(1) Qualitative Observations of Bridging Sites

General observations in our alumina confirm the basic conclusions from earlier studies with optical microscopy.^{4,6} Crack extension occurred in a discontinuous fashion, at load increments from 5 to 15 N, but remained essentially stable during the entire loading, to a maximum level of $\approx 300\ \text{N}$. The fracture mode was predominantly intergranular. Active grain bridges were observed along the entire crack trace and over the entire propagation distance. No indication of a microcrack-cloud zone was observed, even though secondary cracking of grain facet dimensions adjoining the primary crack interface was readily discernible (see below).

Specific examples of SEM observations in the alumina are shown in Figs. 2 and 3. Figure 2 shows a bridging site in the crack wake some $1300\ \mu\text{m}$ behind the tip. That associated wake closure forces must be operative is immediately appar-

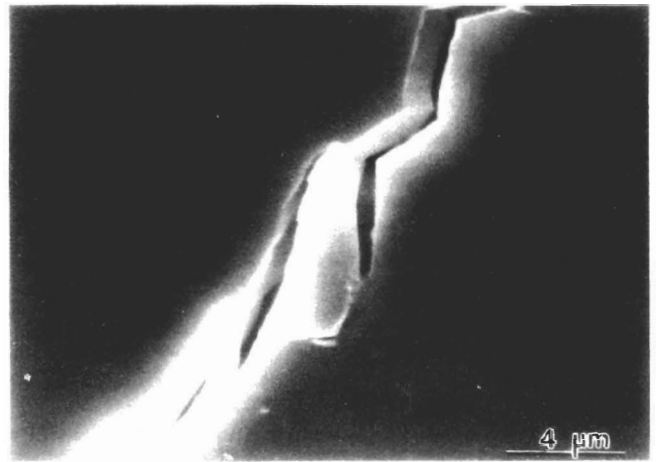


Fig. 2. SEM micrograph showing grain-bridging element at crack interface $1260\ \mu\text{m}$ behind the crack tip. Note resolution of crack-opening displacement.

ent from the severe disruption of individual grains at and around the bridge sites. The capacity to resolve and measure CODs is also clear from this micrograph.

Figure 3 depicts successive views of a second region, at two stages in the applied loading. The distances of this region behind the crack tip at these two stages are $660\ \mu\text{m}$ in Fig. 3(a)

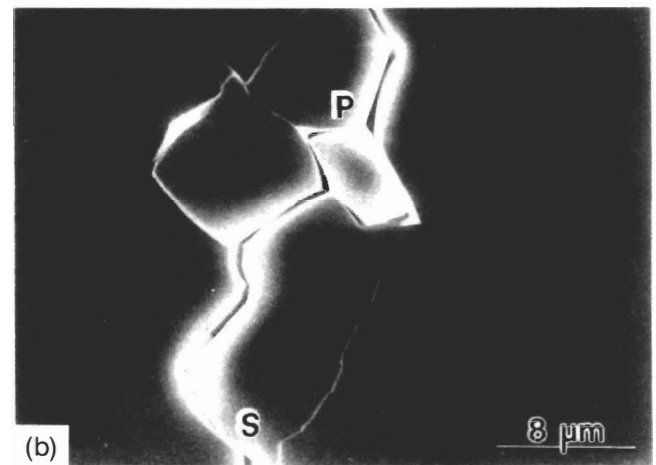
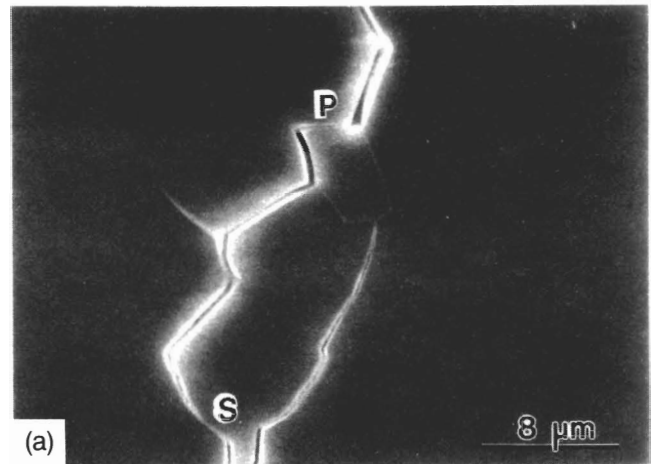


Fig. 3. SEM micrographs showing another grain-bridging element at crack interface at two stages in the loading, (a) 660 and (b) $1190\ \mu\text{m}$ behind the crack tip. P and S denote frictional contact points.

[†]Sumitomo AKP-HP grade (99.995% pure, $0.5\ \mu\text{m}$ crystallites), Sumitomo Chemical America, New York, NY.

and 1190 μm in Fig. 3(b). Two persistent contact points, at P and S, are indicated. At some load between (a) and (b) frictional tractions at P have opened up a network of secondary microfractures adjoining both sides of the primary crack interface. At S a single secondary microfracture has developed in the large grain at right prior to (a). Note that this latter microfracture has closed significantly between (a) and (b), indicating a falloff of the frictional tractions. The grain at S may conveniently be viewed as a fixed-end cantilever beam whose deflection reflects the magnitude of the internally applied friction force.

By contrast, the cracks in the soda-lime glass propagated relatively smoothly, but at a steady rate (typically, $\approx 1 \mu\text{m} \cdot \text{s}^{-1}$) at fixed load, indicating the presence of slow crack growth even under vacuum.¹² Reducing the applied load on the specimen by about 5% was sufficient to bring the crack system to equilibrium.

(2) Quantitative Measurements of Crack-Opening Displacements

CODs, $2u(x)$, were measured for our specimens, with x the distance behind the crack tip as indicated in the schematic of Fig. 4. Figures 5 and 6 show results from repeated crack propagation runs on the glass controls and the alumina, respectively.

The near-tip profiles for stress-free crack surfaces are usually represented by the Irwin K -field plane-strain displacement relation¹³

$$u(x) = (8x/\pi)^{1/2} K_A / E' \tag{1}$$

where $E' = E/(1 - \nu^2)$ in plane strain, E is Young's modulus (400 GPa for alumina and 70 GPa for glass), ν is Poisson's ratio (taken as 0.25 for both materials), and K_A is the applied stress-intensity factor. Equation (1) may be expected to remain a reasonable approximation for nonbridged cracks extending from sufficiently long notches ($\Delta c \ll c_0$, Fig. 4). A parabolic data fit may therefore be used to determine K_A .¹⁴ For the glass in Fig. 5 a profile corresponding to $K_A = 0.56 \text{ MPa} \cdot \text{m}^{1/2}$ (i.e., a little below the reported value $0.7 \text{ MPa} \cdot \text{m}^{1/2}$ for crack propagation at velocity $1 \mu\text{m} \cdot \text{s}^{-1}$ under vacuum¹²) passes through the data.

For alumina in Fig. 6, on the other hand, no such fit is possible with a single value of K_A . Bridging tractions in this material appear to have a strong modifying influence on the crack profile. The solid curve through the data is a theoretical fit allowing for this influence, to be described in Section III(3). We see that the profile in this material is closer to linear than parabolic. Included as the dashed curves in

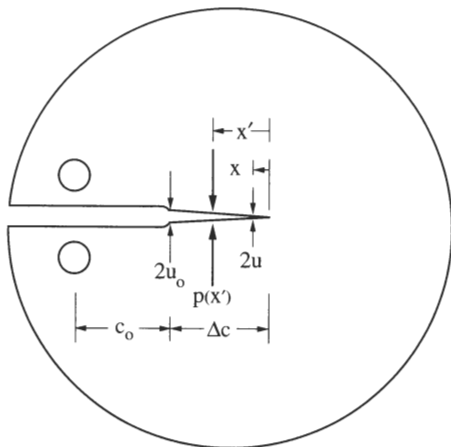


Fig. 4. Schematic of compact-tension specimen. Notch length c_0 , crack extension Δc . Crack profile measured by COD $2u$ at distance x behind crack tip, $2u_0$ at crack mouth. Bridging tractions $p(x')$ act to restrain crack.

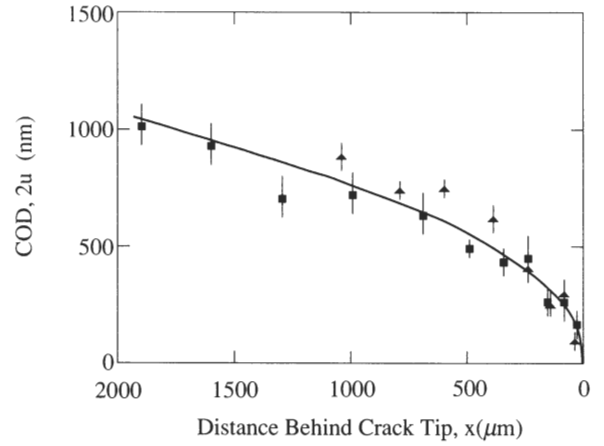


Fig. 5. Measured COD at crack interface in soda-lime glass, for compact-tension specimen ($\Delta c = 1.9 \text{ mm}$). Different symbols designate separate crack runs. Error bars represent systematic uncertainty in COD measurement. Curve is Irwin parabola from Eq. (1) at $K_A = 0.56 \text{ MPa} \cdot \text{m}^{1/2}$.

Fig. 6 are asymptotic parabolas according to Eq. (1) with $K_A = 4.6 \text{ MPa} \cdot \text{m}^{1/2}$ at the crack mouth (notch tip) (evaluated from the externally measured load using a stress-intensity factor solution for compact tension specimens at $\Delta c = 1.0 \text{ mm}$ ⁸) and $2.0 \text{ MPa} \cdot \text{m}^{1/2}$ at the crack tip (corresponding to the grain-boundary toughness, T_0 for alumina⁵).

We reiterate that the COD data in Figs. 5 and 6 correspond to measurements along the crack plane at stationary crack length ($\Delta c = 1.9 \text{ mm}$). Alternatively, one may monitor the COD at the stationary notch tip as a function of variable crack extension Δc . Results of such measurements for the alumina are presented in Fig. 7.

(3) Numerical Calculation of Closure Stresses in the Crack Wake

We indicated above that the crack profile in alumina deviates from the standard parabolic profile because of bridging tractions effective at the crack walls. The profile may thereby be used to compute the magnitude of these bridging tractions via an integral equation for continuum slit cracks.^{17,18} In the limit of small bridging zones ($\Delta c = 1.9 \text{ mm} \ll c = 22 \text{ mm}$)

⁸Using the formula for standard circular specimens,¹⁵ but with a correction factor allowing for nonstandard load-point positions from a general solution for rectangular specimens.¹⁶

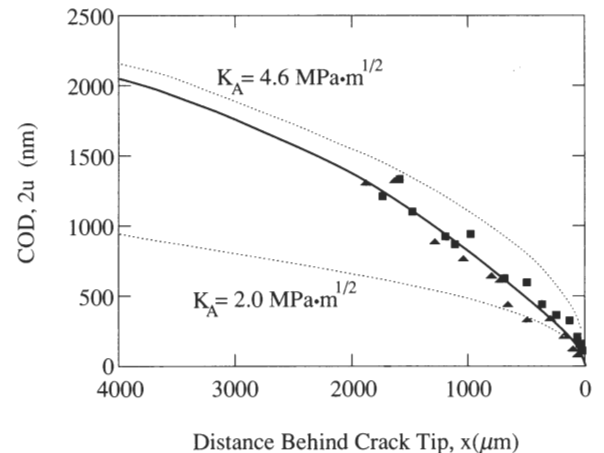


Fig. 6. Measured COD at crack interface in alumina, compact-tension specimen ($\Delta c = 1.9 \text{ mm}$). Fitted profile (solid curve) from Eq. (2), Irwin parabolas for $K_A = 4.6 \text{ MPa} \cdot \text{m}^{1/2}$ and $T_0 = 2 \text{ MPa} \cdot \text{m}^{1/2}$ (dashed curves) from Eq. (1).

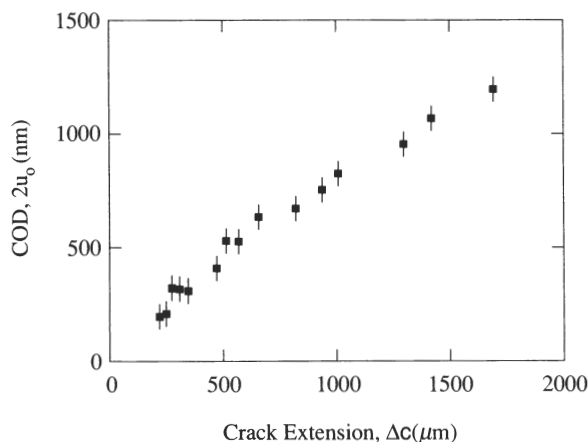


Fig. 7. COD at crack mouth as a function of crack extension for alumina compact-tension specimen.

the profile may be approximated by the Barenblatt relation¹⁷ for cracks under applied stress

$$u(x) = (8x/\pi)^{1/2} K_A/E' - (2/\pi E') \times \int_0^{\Delta c} p(x') \ln [(x'^{1/2} + x^{1/2})/(x'^{1/2} - x^{1/2})] dx' \quad (2)$$

with x a field point at which the displacement is to be evaluated and x' a source point for the stresses $p(x')$.

The problem now consists of finding a solution for a stress function $p(x')$ consistent with the measured profile in Fig. 6. Generally, Eq. (2) is analytically untractable, so numerical analysis is required. To facilitate such an analysis, the stress function was taken to have the empirical “tail-like” form^{5,7}

$$p(x') = p_M(1 - x'/\Delta c_\infty)^n \quad (3)$$

with p_M the peak stress, Δc_∞ the bridging zone size at steady rate, and n an exponent. Note that this function has limiting values $p = p_M$ at $x' = 0$ ($u = 0$) and $p = 0$ at $x' = \Delta c_\infty$ ($u = u_0$), and that n will generally be expected to vary with Δc . Starting with initial estimates from Ref. 7 for p_M and Δc_∞ at $n = 1$ for an alumina with our grain size, iterative parametric adjustments were made to the stress function in Eq. (3) until the calculated crack profile $u(x)$ in Eq. (2) deviated from the (smoothed-out) data set in Fig. 6 by less than a prescribed amount (30 nm) at any position x . This procedure yielded final values $p_M = 70$ MPa, $\Delta c_\infty = 2.5$ mm, and $n = 2.5$ for the half-chevron crack at $\Delta c = 1.9$ mm. The ensuing $u(x)$ function is represented as the smooth curve in Fig. 6.

Figure 8(a) plots the appropriately calibrated stress function $p(x')$ in Eq. (3). The closure stresses decay from ≈ 70 MPa at the crack tip to ≈ 2 MPa at the crack mouth (notch tip). The corresponding stress-separation function $p(u)$ in Fig. 8(b) is obtained in conjunction with Eq. (2). The crack-opening displacement at the notch tip corresponding to $\Delta c = 1.9$ mm is $2u_0 = 1300$ nm.

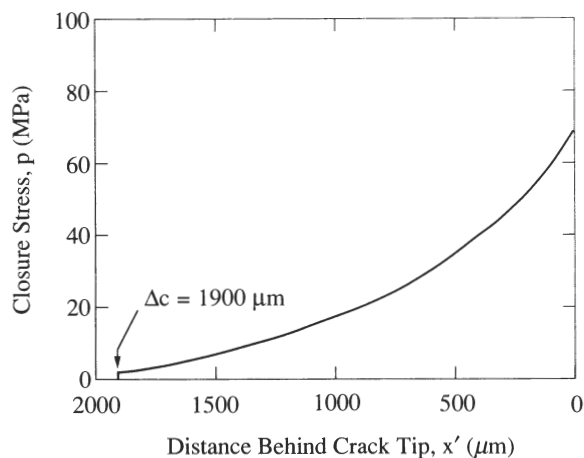
(A) Calculations of the Crack-Tip Shielding Toughness and the R-Curve

Given the calibrated stress functions $p(x')$ and $p(u)$, we may calculate the shielding contribution to the toughness.

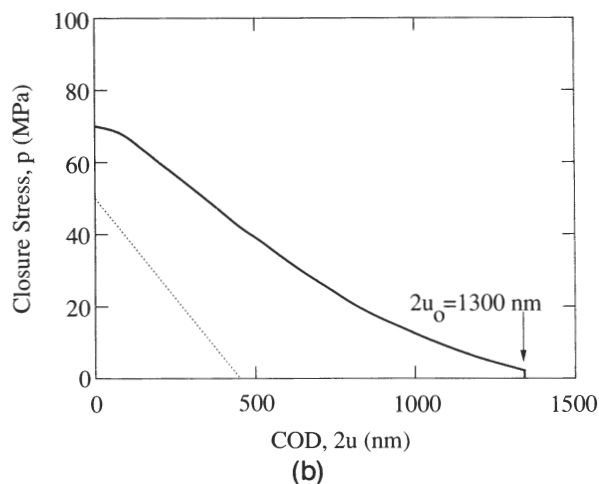
Let us do this first for the crack of fixed size $\Delta c = 1.9$ mm ($2u_0 = 1300$ nm) in Fig. 6. We may do this in two ways:

(A) *Stress-Intensity Factor:* The material toughness consists of superposable contributions from the intrinsic (grain boundary) cohesive forces, T_0 , and the extrinsic microstructural shielding, T_μ . At equilibrium, the net toughness balances the applied K -field:¹⁹

$$K_A = T = T_0 + T_\mu \quad (4)$$



(a)



(b)

Fig. 8. Bridging stress functions: (a) $p(x')$ for compact-tension crack and (b) corresponding $p(u)$, for alumina. Note cutoff in plots at $\Delta c = 1.9$ mm, $2u_0 = 1.3$ μm , indicating limits of crack size over which COD data were obtained in our experiments. Dashed line in (b) is evaluation from indentation-strength data on other aluminas.²⁵

The shielding term may be determined from the Green's function relation¹³

$$T_\mu = (2/\pi)^{1/2} \int_0^{\Delta c} p(x') dx'/x'^{1/2} \quad (5)$$

Numerical integration gives $T_\mu = 2.6$ MPa \cdot m^{1/2} for $\Delta c = 1.9$ mm. This result compares with the value $T_\mu = K_A - T_0 = 4.6 - 2.0 = 2.6$ MPa \cdot m^{1/2} from the asymptotic curves in Fig. 6.¹

(B) *Mechanical-Energy Release Rate:* The equilibrium relation Eq. (4) may be alternatively expressed as a balance between the applied mechanical-energy-release rate, G_A , and the net crack-resistance energy, R :

$$G_A = R = R_0 + R_\mu \quad (6)$$

The shielding term is readily found from^{19,20}

$$R_\mu = 2 \int_0^{u_0} p(u) du \quad (7)$$

Numerical integration gives $R_\mu = 41.8$ J \cdot m⁻². The values

¹⁹Note that application of Eq. (5) to compute T_μ at any other Δc would strictly require reevaluation of Eq. (3), specifically n , at that specific Δc .

thus obtained can be checked for self-consistency through the equivalence relations²¹

$$G_A = K_A^2/E' \quad (8a)$$

$$R_0 = T_0^2/E' \quad (8b)$$

Eliminating G_A and K_A using Eqs. (4) and (6), and inserting the above value of R_μ obtained from Eq. (7) along with the previously cited E' and T_0 for our alumina, we obtain $T_\mu = (T_0^2 + E'R_\mu)^{1/2} - T_0 = 2.7 \text{ MPa} \cdot \text{m}^{1/2}$, which compares with the value 2.6 from Eq. (4).

Now let us consider how we may determine the R -curve from the above analysis. From Eq. (7), R_μ , hence R , may be evaluated directly as the area under the $p(u)$ curve in Fig. 8(b). Numerical integration yields the function $R(u)$ in Fig. 9(a). This result may be converted to the more familiar R -curve function $R(\Delta c)$ using the data points from Fig. 7. That function is plotted in Fig. 9(b). Note that since $p(u)$ is an intrinsic material function, $R(u)$ is a unique quantity for our alumina; but $R(\Delta c)$, insofar as it may be dependent on the crack-profile relation $u(\Delta c)$, is specific to our crack geometry.

IV. Discussion

We have sought to demonstrate that useful qualitative and quantitative information concerning the micromechanics of crack-tip shielding by grain bridging in monophase ceramics can be gained from in situ observations in the SEM. The most immediate outcome from our crack-interface observations on alumina is the confirmed existence of such bridging, shown pictorially in Figs. 2 and 3 and graphically in Fig. 9. Such

observations usefully reinforce earlier inferences as to the efficacy of bridging as a toughening mechanism from the classic wake sawcut experiments of Knehan and Steinbrech.²² They also allow us to make useful inferences concerning the micromechanics of grain pullout; recall our description of secondary fractures (fortuitous "internal load cells") in Fig. 3, indicative of a falloff in frictional force with increasing crack-wall separation.

Our results in Fig. 6 also show that (within experimental scatter) the crack profile at the bridged interface is closer to linear than parabolic. This is in keeping with studies on bridged cracks in fiber-reinforced cementitious composites.²³ An empirical linear COD relation is therefore probably most appropriate for incorporation into fracture mechanics models of bridging zones for R -curve (T -curve) analysis.^{5,7,24}

It will be noted that evaluation of the equilibrium crack profile in Eq. (2) requires specification of K_A for the half-chevron crack. K_A determines the scale of the shielding zone displacement field, thereby avoiding the necessity of making COD measurements in the notch region. Alternatively, one could eliminate K_A altogether from Eq. (2) by substitution of Eqs. (4) and (5):

$$u(x) = (8x/\pi)^{1/2} T_0/E' + (4/\pi E') \int_0^{\Delta c} p(x') \{(x/x')^{1/2} - \frac{1}{2} \ln [(x'^{1/2} + x^{1/2}) / (x'^{1/2} - x^{1/2})]\} dx' \quad (9)$$

so that, given only the intrinsic toughness term T_0 , one may compute the profile without having to evaluate the applied stress-intensity factor. This is a special advantage in those cases where the macroscopic crack geometry is ill-defined. It must be reiterated that the validity of Eq. (9) is contingent on satisfaction of the small-scale bridging zone approximation, $\Delta c \ll c$, and therefore contains no specific information on the profile in the far field.

These considerations open the way to evaluation of T_0 from the COD data. In cases (like ours) where intergranular fracture dominates, this quantity relates to the basic surface and grain-boundary energies, γ_s and γ_{GB} , via $T_0 = [(2\gamma_s - \gamma_{GB}) E']^{1/2}$;²¹ the relative values of γ_{GB} and γ_s (among other things) determine whether a crack will or will not remain along an intergranular path (and hence preserve the most favorable conditions for bridge formation). Access to T_0 is restricted in conventional precrack test procedures because pop-in generally starts the system well up the R -curve. In principle, T_0 should be determinable from the lower bound of the data in Fig. 6, which reflects COD measurements taken within two or three grains behind the crack tip (i.e., within a typical bridge spacing). Thus in Fig. 6 we are able to estimate $T_0 \approx 2.0 \text{ MPa} \cdot \text{m}^{1/2}$ for our alumina. In our case experimental scatter limits the accuracy of this approach, but optimization of the SEM resolution may provide useful estimates in materials with stronger R -curves.

Perhaps the most consequential result from the COD data in Figs. 6 and 7 is the evaluation of the bridging stress functions $p(u)$ and $p(x')$. Notwithstanding the fact that our parametric fitting procedure is constrained by the empirical relation in Eq. (3), the data confirm the existence of a "tail-dominated" constitutive relation, Fig. 8; i.e., maximum restraint at the crack tip, with near-linear falloff along the crack-wake interface. Our $p(u)$ function may be compared with an independent, indirect determination from indentation-strength data on other aluminas, shown as the dashed line in Fig. 8.²⁵ The present evaluation indicates a substantially greater toughening due to bridging; the discrepancy may reflect material-to-material variations and/or uncertainties in deconvoluting the indentation data.²⁵ Once $p(u)$ is established, the R -curve can be determined from Eqs. (6) and (7). The ensuing $R(u)$ and $R(\Delta c)$ functions in Figs. 9(a) and (b) show an initial sharp rise from $\approx 10 \text{ J} \cdot \text{m}^{-2}$ at small crack

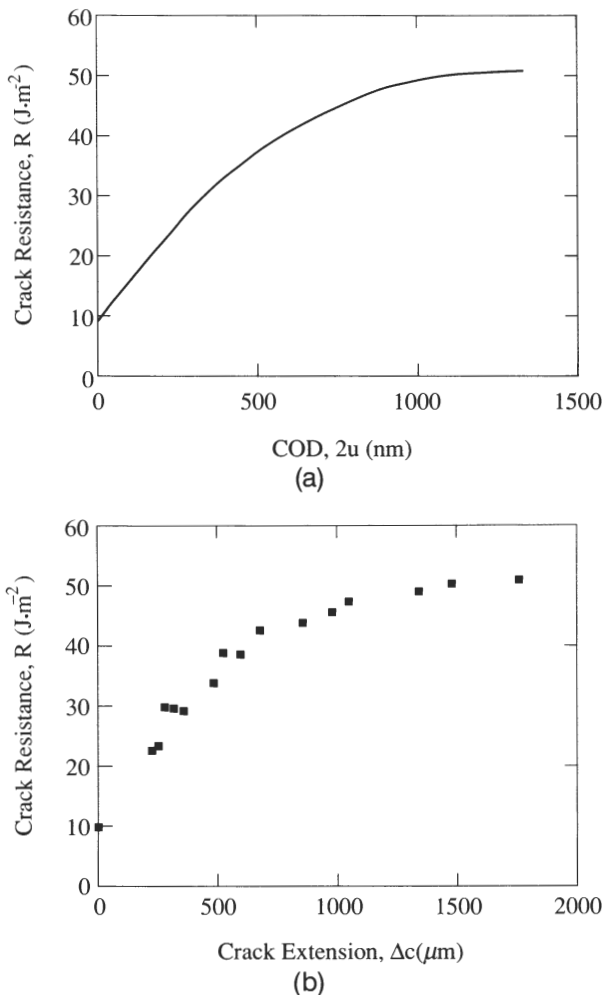


Fig. 9. Crack-resistance curves: (a) $R(u)$ and (b) $R(\Delta c)$ for compact-tension crack ($\Delta c = 1.9 \text{ mm}$) for alumina.

openings (or extensions), to an asymptotic plateau $\approx 50 \text{ J} \cdot \text{m}^{-2}$ at large openings (extensions). (The true plateau value could not be obtained in this study, because the crack size range covered in Figs. 6 and 7 did not extend beyond the range of the bridging zone.)

It is important to acknowledge possible sources of systematic error in the stress-function and R -curve evaluations in Figs. 8 and 9. In using Eq. (2) we have ignored the influence of finite notch length and outer specimen dimensions in our quasi-chevron configuration. Detailed analyses show that boundary effects can be significant in determining displacement profiles in the compact-tension geometry, especially with short notches.²⁶ Also, we have not addressed the possible influence of path deflections (with their connotation of shear modes) on the normal crack displacements.

The present study has focused on a monophase ceramic with moderate grain size. Our device would appear to be potentially even more useful for ceramics with coarser microstructures and multiphase composites, where the toughening events are more dramatic and the R -curves more pronounced. Also, attention has been given only to monotonic loading. Observations in cyclic loading could provide useful clues as to fatigue mechanisms, which remain obscure in ceramic materials. Fatigue might be especially important in materials with strong R -curve behavior, due to cumulative damage to bridges on repeated unloading. COD measurements at the crack mouth (or some other stationary point of interest at the crack interface) could provide a quantitative measure of any such degradation with number of cycles.

V. Conclusions

- (i) A device for in situ investigation of crack interfaces in the SEM has been described.
- (ii) Micrographic evidence for evolution of bridging grains in alumina has been presented.
- (iii) COD measurements as a function of both the distance from the crack tip and crack extension have been analyzed for alumina. The data provide a measure of the crack-tip shielding from bridging.
- (iv) The bridging stress functions $p(u)$ and $p(x')$ have been computed self-consistently from the crack profile measurements.
- (v) Crack-resistance functions $R(u)$ and $R(\Delta c)$ have been evaluated from the stress functions.

Acknowledgments: We are indebted to S. J. Bannison and M. R. Stoudt for help in the design of the fracture device, to B. N. Cox for discussions on the bridged-crack profile, and to E. R. Fuller for assistance with the numerical calculation.

References

¹R. M. McMeeking and A. G. Evans, "Mechanics of Transformation Toughening in Brittle Materials," *J. Am. Ceram. Soc.*, **65** [5] 242–46 (1982).

²M. Rühle, A. G. Evans, R. M. McMeeking, P. G. Charalambides, and J. W. Hutchinson, "Microcrack Toughening in Alumina/Zirconia," *Acta Metall.*, **35** [11] 2701–10 (1987).

³D. B. Marshall and A. G. Evans, "Failure Mechanisms in Ceramic-Fiber/Ceramic-Matrix Composites," *J. Am. Ceram. Soc.*, **68** [5] 225–31 (1985).

⁴P. L. Swanson, C. J. Fairbanks, B. R. Lawn, Y.-W. Mai, and B. J. Hockey, "Crack-Interface Grain Bridging as a Fracture Resistance Mechanism in Ceramics: I, Experimental Study on Alumina," *J. Am. Ceram. Soc.*, **70** [4] 279–89 (1987).

⁵Y.-W. Mai and B. R. Lawn, "Crack-Interface Grain Bridging as a Fracture Resistance Mechanism in Ceramics: II, Theoretical Fracture Mechanics Model," *J. Am. Ceram. Soc.*, **70** [4] 289–94 (1987).

⁶P. L. Swanson, "Crack-Interface Traction: A Fracture-Resistance Mechanism in Brittle Polycrystals"; pp. 135–55 in *Advances in Ceramics*, Vol. 22, Fractography of Glasses and Ceramics. American Ceramic Society, Westerville, OH, 1988.

⁷S. J. Bannison and B. R. Lawn, "Role of Interfacial Grain-Bridging Sliding Friction in the Crack-Resistance and Strength Properties of Nontransforming Ceramics," *Acta Metall.*, **37** [10] 2659–71 (1989).

⁸A. Nagy, J. B. Campbell, and D. L. Davidson, "High-Temperature, Cyclic Loading Stage for the Scanning Electron Microscope," *Rev. Sci. Instrum.*, **55** [5] 776–82 (1984).

⁹H. Frei and G. Grathwohl, "Development of a Piezotranslator-based Bending Device for In Situ SEM Investigations of High-Performance Ceramics," *J. Phys. E*, **22** [8] 589–93 (1989).

¹⁰H. Kodama, H. Sakamoto, and T. Miyoshi, "Silicon Carbide Monofilament Reinforced Silicon Nitride or Silicon Carbon Matrix Composites," *J. Am. Ceram. Soc.*, **72** [4] 551–58 (1989).

¹¹J. Rödel, J. F. Kelly, M. R. Stoudt, and S. J. Bannison, "A Loading Device for Fracture Testing of Compact Tension Specimen in the SEM"; to be published in *Scanning Electron Microsc.*

¹²S. M. Wiederhorn, H. Johnson, A. M. Diness, and A. H. Heuer, "Fracture of Glass in Vacuum," *J. Am. Ceram. Soc.*, **57** [8] 336–41 (1974).

¹³G. R. Irwin, "Fracture"; pp. 551–94 in *Handbuch der Physik*, Vol. 6. Springer-Verlag, Berlin, 1958.

¹⁴E. Sommer, "Experimental Determination of Stress Intensity Factor by COD Measurements"; pp. 331–47 in *Mechanics of Fracture*, Vol. 7. Edited by G. C. Sih. Nijhoff Publishers, The Hague, Netherlands, 1981.

¹⁵Annual Book of ASTM Standards, Vol. 3.01, E-399-83; pp. 480–504. American Society for Testing and Materials, Philadelphia, PA, 1989.

¹⁶H. Tada, P. C. Paris, and G. R. Irwin, *The Stress Analysis Handbook*; Ch. 2. Paris Productions (and Del Research Corp.), St. Louis, MO, 1985.

¹⁷G. I. Barenblatt, "The Mathematical Theory of Equilibrium Cracks in Brittle Fracture," *Adv. Appl. Mechan.*, **7**, 55–129 (1962).

¹⁸I. N. Sneddon and M. Lowengrub, *Crack Problems in the Classical Theory of Elasticity*. Wiley, New York, 1969.

¹⁹Y.-W. Mai and B. R. Lawn, "Crack Stability and Toughness Characteristics in Brittle Materials," *Annu. Rev. Mater. Sci.*, **16**, 415–39 (1986).

²⁰J. R. Rice, "Mathematical Analysis in the Mechanics of Fracture"; pp. 191–311 in *Fracture II*. Edited by H. Liebowitz. Academic Press, New York, 1968.

²¹B. R. Lawn and T. R. Wilshaw, *Fracture of Brittle Solids*; Ch. 6. Cambridge University Press, London, 1975.

²²R. Knehan and R. W. Steinbrech, "Memory Effect of Crack Resistance during Slow Crack Growth in Notched Al_2O_3 Bend Specimens," *J. Mater. Sci. Lett.*, **1** [8] 327–29 (1982).

²³B. Cotterell and Y.-W. Mai, "Modelling Crack Growth in Fibre-Reinforced Cementitious Materials," *Mater. Forum*, **11**, 341–51 (1988).

²⁴R. M. L. Foote, Y.-W. Mai, and B. Cotterell, "Crack Growth Resistance Curves in Strain-Softening Materials," *J. Mech. Phys. Solids*, **34** [6] 593 (1986).

²⁵P. Chantikul, S. J. Bannison, and B. R. Lawn, "Role of Grain Size in the Strength and R -Curve Properties of Alumina," *J. Am. Ceram. Soc.*, **73** [8] 2419–27 (1990).

²⁶B. N. Cox and D. B. Marshall, "Stable and Unstable Solutions for Bridged Cracks in Various Specimens; unpublished work. □